Coaxially Conductive Organic Wires through Self-Assembly

Shayan Louie¹, Yu Zhong², Si Tong Bao¹, Cedric Schaack¹, Alvaro Montoya³, Zexin Jin¹, Nicholas M. Orchanian¹, Yang Liu⁴, Wenrui Lei¹, Kelsey Harrison¹, James Hone⁴, Alexander Angerhofer³, Austin M. Evans*^{3,5}, Colin P. Nuckolls*¹

- ¹Department of Chemistry, Columbia University, New York, New York 10027, United States
- ²Department of Materials Science and Engineering, Cornell University, Ithaca, New York 14853, United States
- ³Department of Chemistry, University of Florida, Gainesville, Florida, 32611, United States
- ⁴Department of Mechanical Engineering, Columbia University, New York, New York 10027, United States
- ⁵George & Josephine Butler Polymer Research Laboratory, Center for Macromolecular Science and Engineering, Gainesville, Florida, 32611, United States
- *e-mail: AustinEvans@chem.ufl.edu; cn37@columbia.edu

KEYWORDS: Macrocycles, Electrical Conductivity, Synthetic Nanotubes

ABSTRACT: Here, we describe the synthesis of the hexameric macrocyclic aniline (MA[6]), which spontaneously assembles into coaxially conductive organic wires in its oxidized and acidified emeraldine salt (ES) form. Electrical measurements reveal that ES-MA[6] exhibits high electrical conductivity ($7.5 \times 10^{-2} \text{ S} \cdot \text{cm}^{-1}$) and that this conductivity is acid-base responsive. Single-crystal X-ray crystallography reveals that ES-MA[6] assembles into well-defined trimeric units that then stack into nanotubes with regular channels, providing a potential route to synthetic nanotubes that are leveraged for ion or small molecule transport. Ultraviolet-visible-near-infrared absorbance spectroscopy and electron paramagnetic spectroscopy showcase the interconversion between acidic (conductive) and basic (insulating) forms of these macrocycles and how charge-carriers are formed through protonation, giving rise to the experimentally observed high electrical conductivity.

This manuscript describes a new design motif to create macrocycles that assemble into wires that support both electrical and ionic transport. Materials that possess electrical and ionic conductivity are particularly attractive because of their potential uses in many critical technologies such as electrochemical energy storage, 1,2 catalysis, 3,4 adaptive electronics,5,6 or chemical sensing.7,8 The utility of these motifs is in their coaxial modes of transport: heavy carriers such as ions or protons move through one portion of the material while electrons or holes move through the other portion. The motif that we create here is a macrocycle constructed from para-linked anilines, known as polyaniline (PANI). PANI is a polymer that exhibits high conductivity depending on its oxidation- and protonationstate (Fig. 1A).9 In its oxidized and neutral emeraldine base (EB) form, PANI is found to be diamagnetic and demonstrates low bulk conductivity (10-10 S·cm-1).10,11 When proton doped, PANI converts to a highly conductive (10-2-100 S·cm-1) poly-radicaloid state.9 However, structural and electronic inhomogeneity present in PANI and its derivatives produces several orders of magnitude of variation in the bulk conductivity.10-13 Theoretical studies suggest that macrocyclic oligo-anilines will exhibit delocalization of their frontier orbitals and thus will have more uniform electron distribution and enhanced stability.14,15 There are several studies that create functionalized derivatives of N-containing macrocycles, $^{14,16-22}$ but these macrocycles, due in large part to the tertiary substitution of the heteroatoms or bulky substitution of their backbone, lack the rich redox and pH sensitivity inherent to PANI. 14

Here, we prepare and study for the first time the macrocyclic versions of the oligoanilines, which we have named Macrocyclic Anilines (MAs). The hexameric version of these macrocycles, MA[6], is a prototype of this new motif, containing six para-substituted aryl rings each bridged with secondary nitrogen atoms (Fig. 1B). By using a thermolytic Boc deprotection strategy in the final synthetic step, we circumvent solubility issues that complicate previous synthetic routes. We find that MA[6] can be converted to its "emeraldine salt" (ES-MA[6]) form in the presence of trifluoroacetic acid (TFA) under aerobic conditions, similar to PANI. Crystals and thin films of ES-MA[6] exhibit both ionic and electrical conductivity. Moreover, we find that the conductivity is responsive to pH. X-ray crystallography and electron paramagnetic resonance (EPR) spectroscopy reveal that ES-MA[6] can be isolated in a stable radical state with the charge evenly distributed throughout the backbone. These radicaloids further assemble into well-defined trimeric units that then stack into nanotubes with regular channels.

Figure 1. A) Oxidation/reduction and acid/base switchability of linear polyaniline. **B)** Oxidation/reduction and acid/base switchability of MA[6].

We synthesized MA[6] through an iterative approach with high-yield and purity (**Scheme 1**). The linear precursor was prepared by a sequential S_NAr, Boc-protection, and hydrogenation route. The macrocyclization was performed under dilute (5 mM) conditions via a Buchwald-Hartwig cross-coupling with a 28% isolated yield. Finally, we thermolytically cleaved the Boc protecting groups by heating **Scheme 1. Synthesis of MA[6].**

the solid Boc-protected MA[6] at 150 °C *in vacuo* for 9 hours. The supporting information contains the details for the characterization of MA[6] and its precursors. This expeditious synthesis is both scalable and provides highpurity MA[6], which facilitates its electronic, optical, and magnetic characterization.

Solid-state cyclic voltammograms of MA[6] (**Fig. S1**) demonstrate significant overlapping of oxidation peaks as opposed to the distinct redox features observed in previously studied *N*-substituted macrocycles.^{14,17,19,21,22} We attribute the differences in the CV's to strong coupling of redox events in MA[6] and the presence of amine protons that become mobile/immobile upon oxidation/reduction, which is a common feature of PANI electrochemistry.¹¹ There is also a scan-rate dependence on the number of observable redox events as the three oxidation features observed at 20 mV/s converge with increasing scan rate, which suggests that there is some structural/chemical change occurring during the slow scan rate studies such as isomerization/planarization/de-planarization after the

first oxidation event which enables a second oxidation. We also note that the voltage difference between oxidations and reductions are large (250 mV for the first reduction/oxidation pair) which is likely due to diffusion-like transport of electrons through the molecular film, a common occurrence for electroactive polymer films. 11,23

Single-crystals of MA[6] were produced by slow evaporation of heptane into 5% trifluoroacetic acid/acetonitrile and solid zinc over the course of three days. Single-crystal structures reveal that MA[6] is a hexagonal, rigidly planar macrocycle (**Fig. 2A**), consistent with ¹H and ¹³C nuclear magnetic resonance spectroscopy (**Fig. S4 & S5**) and high-resolution mass spectrometry characterization. Having produced these crystals under acidified conditions with

zinc, the doubly oxidized "emeraldine salt" version of these materials was isolated as a co-crystal with Zn[CF₃CO₂]₂. Both the macrocycles and zinc are oxidized to the 2+ state by oxygen present under acidic aerobic conditions, consistent with the well-studied polyaniline systems. Based on the bond lengths between observed by single-crystal X-ray diffraction, it appears that the positive charges are shared evenly amongst the six nitrogen centers in each macrocycle (Fig. 2B & S6). This observation is consistent with previous theoretical calculations that suggest the frontier orbitals in macrocyclic polyanilines should be evenly spread amongst the electronically coupled nitrogen centers. 14,15 This is in contrast to linear oligo [n] aniline systems, which have an uneven dispersion of charge density due to the different on-site energies of N-sites in a linear chain (e.g. at chain ends). Doubly oxidized macrocycles assemble into trimers in the solid-state. We hypothesize that these six

charge-carriers are delocalized across the trimeric assembly, which likely further improves the stability and electronic mobility of this system. This hypothesis is consistent with the tight π - π stacking distances (3.68-4.27 Å centroid-centroid separations) observed in these trimeric assemblies (Fig. 2C & S7). ES-MA[6] trimer assemblies are further stabilized by a network of hydrogen-bonding interactions with the carboxylate group of inner channel TFA anions sandwiched by neighboring trimers and by outer channel TFA anions surrounding the zinc clusters (Fig. 2A & 2D). Together, these interactions lead to the formation of synthetic nanotubes in the long-range with well-defined channels (Fig. 2A & 3D). Single-crystal X-ray diffraction resolves that covalent and non-covalent interactions lead to spontaneous structural ordering at the molecular, fewmolecule, and long-range length scales.

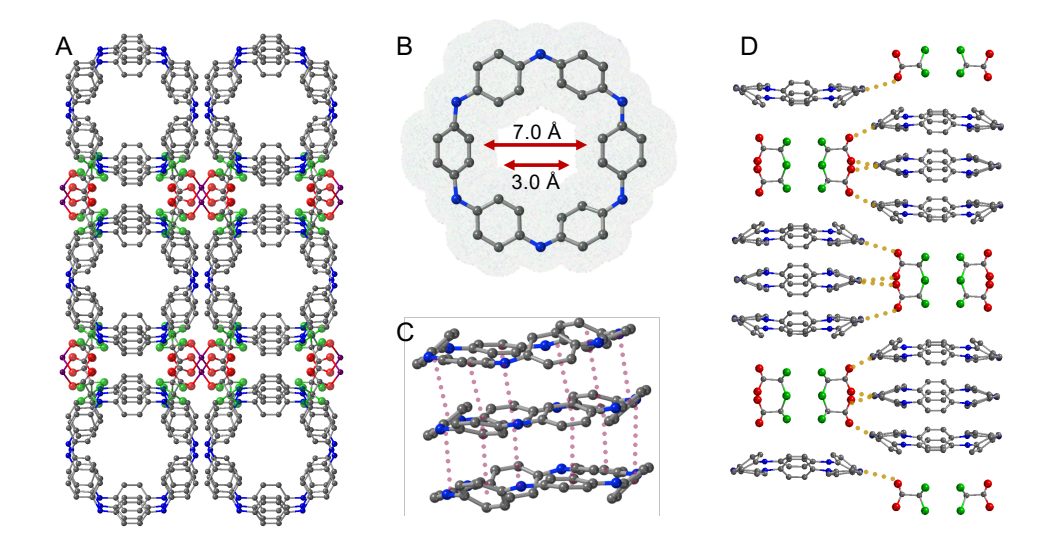


Figure 2. A) Top-view X-ray structures of ES-MA[6] and outer channel zinc clusters. Hydrogen atoms and inner channel TFA anions omitted for clarity. C, N, O, F, and Zn atoms are colored in gray, blue, red, green, and purple, respectively. **B)** Top-view of ES-MA[6] and its Van der Waals surface. **C)** Side view of ES-MA[6] trimers with π - π interactions highlighted by red lines. **D)** Side-view X-ray structures of ES-MA[6] and inner-channel TFA anions. Hydrogen bonds between ES-MA[6] and TFA anions are highlighted by yellow lines. Hydrogen atoms and outer channel Zn clusters omitted for clarity.

The presence of charge-carriers and nanotubular stacking observed in the ES-MA[6] crystal structure encouraged us to investigate its electronic and ionic transport properties as films and as single crystals. Techniques including powder x-ray diffraction (Fig. S11), atomic force microscopy (Fig. S12), and scanning electron microscopy (Fig. S14), confirm the formation of nano-wires in thin films of ES-MA[6] and reinforce that the nanotube assembly is the dominant motif in this material, promising the potential for charge transport.

We fabricated devices by spin casting films of ES-MA[6], on Si/SiO₂ wafers, followed by deposition of Ag or Au contacts with a shadow mask. Two-contact conductivity measurements determined the bulk conductivity of the devices with Ag contacts to be 7.0×10^{-5} S·cm⁻¹ and the devices with Au contacts to be 1.7×10^{-5} S·cm⁻¹ (**Fig. S20**). Higher currents were observed for devices made with Ag contacts compared to Au contacts, which we attribute to a lower interfacial resistance and stronger interaction between Ag

and the film. Additionally, four-contact measurements on devices with Ag contacts revealed an even higher conductivity value of $4.7\times10^{-4}~\rm S\cdot cm^{-1}$ (Fig. S22).

We prepared single crystal devices by growing crystals of ES-MA[6] on Si/SiO2 wafers, followed by deposition of Ag contacts with a shadow. Comparing the dimensions of the crystals used for X-ray diffraction with those grown on Si/SiO₂ confirmed conductivity measurements through stacked macrocycles. Although there are gaps between the macrocycle trimers, there is also tight packing between neighboring trimers in the diagonal direction that can still allow for anisotropic charge transport. Single-crystal devices prepared this way had a measured conductivity of $7.5 \times 10^{-2} \text{ S} \cdot \text{cm}^{-1}$ (Fig. 3A), which is over two orders of magnitude higher than our four-contact conductivity values and approximately three orders of magnitude higher than comparable two-probe thin film devices. Using the crystal structure calculated density of 1.33 g·cm⁻³, we determined that ES-MA[6] has a charge-carrier density of 1.1 $\times~10^{21}$ carriers·cm⁻³. These measurements demonstrate that significant electronic conductivities can be achieved by concurrently controlling multiple length scales. The conductivity of ES-MA[6] rivals that of other well-established polymeric conductors such as polythiophene $(10^0-10^3~{\rm S\cdot cm^{-1}}),~{\rm polyaniline}~(10^{-2}-10^0~{\rm S\cdot cm^{-1}}),~{\rm or}~{\rm polypyrrole}~(10^0-10^1~{\rm S\cdot cm^{-1}}).^9$ However, these macrocycles feature a well-defined size and structure, affording greater precision in the self-assembly into films or crystals.

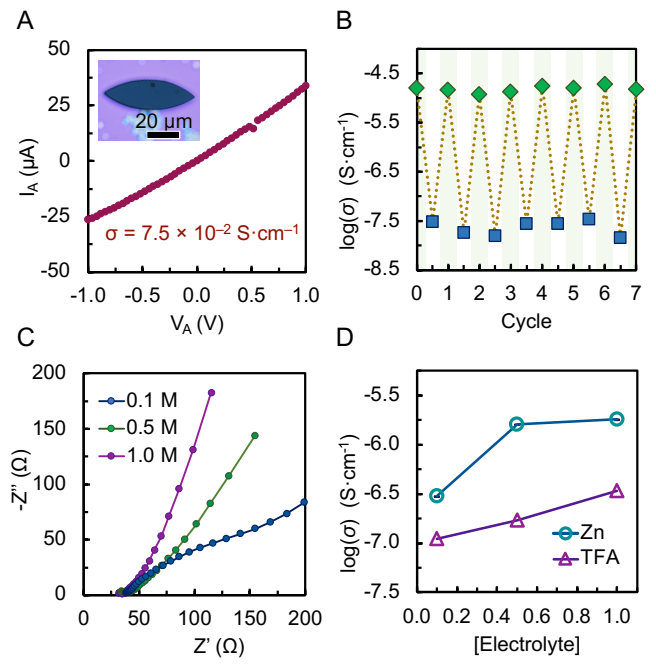


Figure 3. A) Plot of current vs. voltage for single crystal conductivity measurement of ES-MA[6] with Ag contacts. **B)** Conductivity of an ES-MA[6] device when alternatively immersed in aqueous solutions of trifluoroacetic acid (green diamond) and ammonia (blue squares) over 7 cycles. **C)** Nyquist plot showing impedance of ES-MA[6] at various concentrations of Zn[CF₃CO₂]₂. **D)** Plot of concentration vs. ionic conductivity for ES-MA[6] at various concentrations of Zn[CF₃CO₂]₂ (turquoise circles) and CF₃CO₂H.

We next explored the pH dependence of MA[6]'s electrical conductivity. Given that proton-doping leads to high conductivities, it was hypothesized that de-doping using base

would cause a decrease in conductivity. After exposing an Au contact thin film device with an initial conductivity of $1.6 \times 10^{-5}~\rm S\cdot cm^{-1}$ to a 1.0 mM aqueous solution of NH₃ (pH = 10), we observed over a 400-fold decrease in conductivity ($3.0 \times 10^{-8}~\rm S\cdot cm^{-1}$) (**Fig. 3B**). Following re-exposure of the basified device to a 1.0 M aqueous solution of trifluoroacetic acid (TFA) (pH < 1), we observed a recovery of the electronic conductivity ($1.5 \times 10^{-5}~\rm S\cdot cm^{-1}$). This process was generally reversible for at least 7 cycles, demonstrating that the conductivity of MA[6] is both switchable and reversible, opening up future possibilities of incorporating these molecules in applications such as chemical detectors or neuromorphic memory devices.

High electrical conductivities in an inherently tubular structure inspired studies into the movement of ions in MAs. In particular, we were interested in studying the interactions between MA[6] and zinc due to the presence of Zn²⁺ in the exterior pores of the macrocycles as observed through x-ray diffraction. We utilized a 3 electrode system consisting of ES-MA[6] on ITO glass as the working electrode with an Ag/AgCl reference electrode and a Pt counter electrode (Fig. S25). An aqueous electrolyte solution was added to the cell and electrochemical impedance spectra (EIS) were collected from 100 kHz to 0.1 Hz at a 10 mV amplitude (Fig. 3C). Impedance measurements were obtained at three different concentrations of Zn[CF₃CO₂]₂, which was compared to the same concentrations of TFA. Nyquist plots for all TFA solutions formed a semicircular curve (Fig. S26) whereas those containing Zn[CF₃CO₂]₂ (Fig. 3C) had the distinct shape of a Warburg element often associated with ion diffusion.²⁴ Using a transmission line model,²⁵⁻²⁷ we obtained conductivity values as high as $1.8 \times 10^{-6} \text{ S} \cdot \text{cm}^{-1} \text{ in } 1.0 \text{ M Zn}[\text{CF}_3\text{CO}_2]_2 \text{ compared to } 3.4 \times 10^{-6} \text{ S} \cdot \text{cm}^{-1} \text{ in } 1.0 \text{ M Zn}[\text{CF}_3\text{CO}_2]_2 \text{ compared to } 3.4 \times 10^{-6} \text{ S} \cdot \text{cm}^{-1} \text{ in } 1.0 \text{ M Zn}[\text{CF}_3\text{CO}_2]_2 \text{ compared to } 3.4 \times 10^{-6} \text{ S} \cdot \text{cm}^{-1} \text{ in } 1.0 \text{ M Zn}[\text{CF}_3\text{CO}_2]_2 \text{ compared to } 3.4 \times 10^{-6} \text{ S} \cdot \text{cm}^{-1} \text{ in } 1.0 \text{ M Zn}[\text{CF}_3\text{CO}_2]_2 \text{ compared to } 3.4 \times 10^{-6} \text{ C}_2 \text{ Compared to } 3.4 \times 10^{-6} \text{ C}_2 \text{$ 10⁻⁷ S⋅cm⁻¹ in 1.0 M TFA (Fig. 3D). Although a solution of Zn[CF₃CO₂]₂ should have approximately 1.5 times more solvated ions compared to TFA at a given concentration, Zn[CF₃CO₂]₂ provided higher conductivities at both 0.5 M and 1.0 M than TFA which support the hypothesis that Zn ions are diffusing through ES-MA[6]. Together, electronic and ionic conductivity studies confirm the mixed-ionic electronic behaviors observed in macrocyclic anilines and highlight the significance of these materials for applications in electrochemical devices.

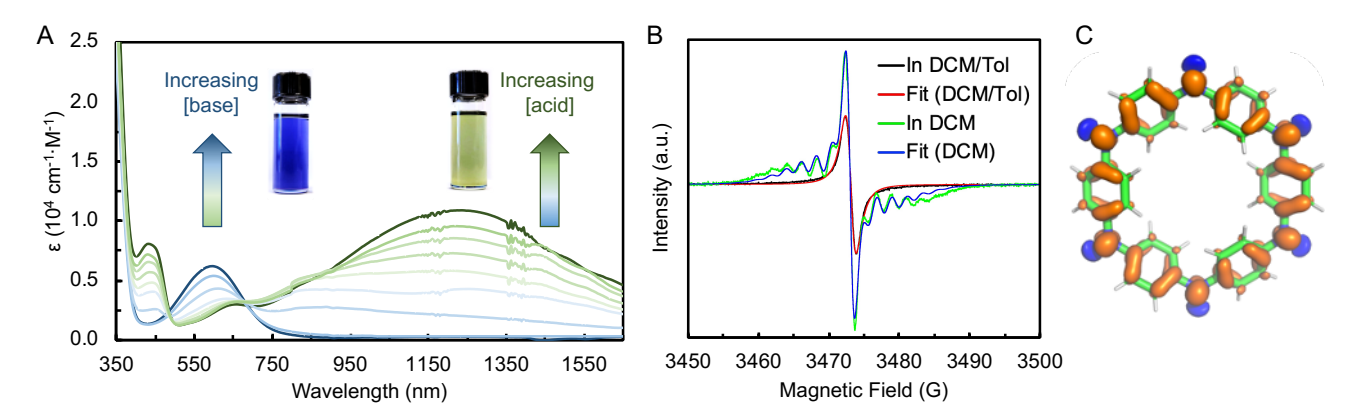


Figure 4. A) UV-vis-NIR absorbance spectrum of MA[6] in DMSO in the presence of TFA (green) and triethylamine (blue). Photo insert visually demonstrates the color difference between acidified ES-MA[6] (right) and basified EB-MA[6] (left). **B)** EPR spectra

of ES-MA[6] in neat DCM (green trace) and in a 1:1 (vol) mixture of DCM and toluene (black trace) together with their corresponding simulations (blue trace – neat DCM; red trace – DCM/toluene mixture). **C)** Calculated spin densities with α -spin density in orange and β -spin density in blue.

We use spectroscopic measurements to follow the acid/base response of the electronic properties of MA[6]. Ultraviolet-visible-near-infrared (UV-vis-NIR) absorption spectroscopy demonstrates that in the presence of an acid, ES-MA[6] has an absorbance maximum at 1270 nm that is indicative of a polaronic transition (**Fig. 4A**) as has been observed in previous highly conductive linear polyaniline systems.²⁸⁻³⁰ Addition of triethylamine induces a new absorption band centered at 600 nm, indicating that the bandgap of the material has increased. When modulating the acid/base concentration of the solution, isosbestic points are observed at 490 nm and 690 nm, demonstrating an interconversion between two different species, which is in agreement with our observations regarding the acid/base switchability of MA[6].

Electronic paramagnetic resonance (EPR) spectroscopy reveals that unpaired charge-carrier densities are enhanced upon protonation and diminish with deprotonation. EB-MA[6] in basic solution of dichloromethane (DCM) had no measurable EPR signal, consistent with the presence of the expected diamagnetic species (Fig. S27). In contrast, upon TFA addition, a strong signal with a *g*-factor of 2.002 and a multiplet hyperfine structure is observed, consistent with the presence of an organic radical (Fig. 4B & S28). When ES-MA[6] is placed in a DCM/toluene mixture small microcrystals form (Fig. S29). This changes the EPR spectrum dramatically, revealing a single Lorentzian line at the same *g*-value due to the presence of strong spinspin coupling in the solid state (Fig. 4B). The spectrum of ES-MA[6] in neat DCM is a composite of individually dissolved cation radicals with a broad hyperfine resolved EPR signature and small microcrystals with a single EPR line (Fig. 4B). DFT calculations reveal that the six amines are the main contributors to the resolved hyperfine coupling in the spectrum (Fig. 4C). The calculations predict a slightly rhombic g-tensor with the principal values of 2.001978, 2.00326, and 2.00342 which averages to an isotropic gvalue of 2.00289. The predicted isotropic hyperfine coupling constants of the six nitrogens are 4.25 ± 0.02 MHz and of the six hydrogens bonded to the nitrogens -6.96 ± 0.03 MHz (see supporting information for atomic coordinates of the DFT optimized structure of ES-MA[6] and the calculated hyperfine coupling constants to all magnetic nuclei, including ¹³C). These values were found to be only qualitatively consistent with the experimental spectrum and as such a least square fitting routine (function esfit within the Easyspin toolbox for MATLAB)31 was used to optimize the fit which yielded hyperfine coupling constants of a_N = 5.69 MHz and a_H = -6.71 MHz. Our EPR spectra and DFT calculations are in general agreement with those of previously studied N-containing macrocycles which demonstrate that radical charges are evenly distributed throughout the macrocycle backbone. 14,19 Taken together, spectroscopic characterization demonstrates that ES-MA[6] hosts a high charge-carrier density and a small and broad optical bandgap, both of which are consistent with the high experimentally observed conductivities.

In conclusion, this work describes a molecular macrocycle that stacks into tubular structures and demonstrates high conductivity, making it useful in many electrochemical applications. These macrocycles demonstrate acid/base responsiveness, forming stable polyradical systems in their acidified state and diamagnetic systems in their basified form. This switchability can be used to tune the conductivity of the material. Moreover, the synthetic route outlined in this paper enables the formation of a family of different sizes of macrocycles with different ion selectivity.

ASSOCIATED CONTENT

Supporting Information

The Supporting Information is available free of charge on the ACS Publications website.

Synthetic details and characterization, electrochemistry, additional experimental procedures, imaging, X-ray crystallography, EPR spectra, and calculation details.

AUTHOR INFORMATION

Corresponding Author

*austinevans@chem.ufl.edu *cn37@columbia.edu

Author Contributions

The manuscript was written with contributions from all authors. All authors have given approval to the final version of the manuscript.

Funding Sources

 $\mbox{A.M.E.}$ was supported by the Schmidt Science Fellows, in partnership with the Rhodes Trust.

ACKNOWLEDGMENT

C.N. thanks Sheldon and Dorothea Buckler for their generous support. This research was supported by the National Science Foundation under award number CHE-2204008. A.M.E. was supported by the Schmidt Science Fellows, in partnership with the Rhodes Trust. The authors acknowledge the Columbia University Shared Materials Characterization Lab (SMCL), Clean Room, and the Electron Microscopy Lab, managing instrumentation supported by the NSF through the Columbia University, Materials Research Science and Engineering Center under award DMR-2011738. The NMR studies reported in this publication were supported by the Office of the Director, of the National Institutes of Health under Award Number S10OD026749. The content is solely the responsibility of the authors and does not necessarily represent the official views of the National Institutes of Health. We acknowledge Dr. Michael Strauss for helpful discussions regarding the synthesis.

ABBREVIATIONS

EPR: Electron Paramagnetic Resonance HRMS: High resolution-Mass Spectrometry

ME: Macrocyclic Emeraldine NMR: Nuclear Magnetic Resonance

PANI: Polyaniline

UV-vis-NIR: Ultraviolet-Visible-Near-Infrared

REFERENCES

- (1) Beker, P.; Koren, I.; Amdursky, N.; Gazit, E.; Rosenman, G. Bioinspired Peptide Nanotubes as Supercapacitor Electrodes. *J Mater Sci* 2010, 45 (23), 6374–6378. https://doi.org/10.1007/s10853-010-4624-z.
- (2) Ryu, J.; Kim, S.-W.; Kang, K.; Park, C. B. Mineralization of Self-Assembled Peptide Nanofibers for Rechargeable Lithium Ion Batteries. *Adv. Mater.* 2010, 22 (48), 5537–5541. https://doi.org/10.1002/adma.201000669.
- (3) Yang, J.; Dewal, M. B.; Shimizu, L. S. Self-Assembling Bisurea Macrocycles Used as an Organic Zeolite for a Highly Stereoselective Photodimerization of 2-Cyclohexenone. *J. Am. Chem. Soc.* 2006, 128 (25), 8122–8123. https://doi.org/10.1021/ja062337s.
- (4) Wu, S.; Li, Y.; Xie, S.; Ma, C.; Lim, J.; Zhao, J.; Kim, D. S.; Yang, M.; Yoon, D. K.; Lee, M.; Kim, S. O.; Huang, Z. Supramolecular Nanotubules as a Catalytic Regulator for Palladium Cations: Applications in Selective Catalysis. *Angew. Chem. Int. Ed.* 2017, 56 (38), 11511–11514. https://doi.org/10.1002/anie.201706373.
- (5) Barnes, J. C.; Dale, E. J.; Prokofjevs, A.; Narayanan, A.; Gibbs-Hall, I. C.; Juríček, M.; Stern, C. L.; Sarjeant, A. A.; Botros, Y. Y.; Stupp, S. I.; Stoddart, J. F. Semiconducting Single Crystals Comprising Segregated Arrays of Complexes of C 60. J. Am. Chem. Soc. 2015, 137 (6), 2392-2399. https://doi.org/10.1021/ja512959g.
- (6) Zasada, L. B.; Guio, L.; Kamin, A. A.; Dhakal, D.; Monahan, M.; Seidler, G. T.; Luscombe, C. K.; Xiao, D. J. Conjugated Metal-Organic Macrocycles: Synthesis, Characterization, and Electrical Conductivity. J. Am. Chem. Soc. 2022, 144 (10), 4515-4521. https://doi.org/10.1021/jacs.1c12596.
- (7) de la Rica, R.; Mendoza, E.; Matsui, H. Bioinspired Target-Specific Crystallization on Peptide Nanotubes for Ultrasensitive Pb Ion Detection. *Small* 2010, 6 (16), 1753–1756. https://doi.org/10.1002/smll.201000489.
- (8) Hu, Y.; Ma, X.; Zhang, Y.; Che, Y.; Zhao, J. Detection of Amines with Fluorescent Nanotubes: Applications in the Assessment of Meat Spoilage. ACS Sens. 2016, 1 (1), 22–25. https://doi.org/10.1021/acssensors.5b00040.
- (9) Nezakati, T.; Seifalian, A.; Tan, A.; Seifalian, A. M. Conductive Polymers: Opportunities and Challenges in Biomedical Applications. *Chem. Rev.* 2018, 118 (14), 6766–6843. https://doi.org/10.1021/acs.chemrev.6b00275.
- (10) Cao, Y.; Smith, P.; Heeger, A. J. Counter-Ion Induced Processibility of Conducting Polyaniline and of Conducting Polyblends of Polyaniline in Bulk Polymers. *Synthetic Metals* 1992, 48 (1), 91–97. https://doi.org/10.1016/0379-6779(92)90053-L.
- (11) Ziadan, K. M.; Saadon, W. T. Study of the Electrical Characteristics of Polyaniline Prepeared by Electrochemical Polymerization. *Energy Procedia* **2012**, *19*, 71–79. https://doi.org/10.1016/j.egypro.2012.05.184.
- (12) Blinova, N. V.; Stejskal, J.; Trchová, M.; Prokeš, J. Control of Polyaniline Conductivity and Contact Angles by Partial Protonation. *Polym. Int.* 2008, 57 (1), 66–69. https://doi.org/10.1002/pi.2312.
- (13) Jafarzadeh, S.; Thormann, E.; Rönnevall, T.; Adhikari, A.; Sundell, P.-E.; Pan, J.; Claesson, P. M. Toward Homogeneous Nanostructured Polyaniline/Resin Blends. ACS Appl. Mater. Interfaces 2011, 3 (5), 1681–1691. https://doi.org/10.1021/am2002179.
- (14) Ito, A.; Yokoyama, Y.; Aihara, R.; Fukui, K.; Eguchi, S.; Shizu, K.; Sato, T.; Tanaka, K. Preparation and Characterization of N-Anisyl-Substituted Hexaaza[16]Paracyclophane. Angewandte Chemie International Edition 2010, 49 (44), 8205–8208. https://doi.org/10.1002/anie.201002165.
- (15) Zamani, M.; Rezaei, M. Comparative Study of Cyclic Polyaniline Oligomers with Linear and Bent Structures. *Molecular*

- *Physics* **2022**, *120* (7), e2029966. https://doi.org/10.1080/00268976.2022.2029966.
- (16) Yan, X. Z.; Pawlas, J.; Goodson, T.; Hartwig, J. F. Polaron Delocalization in Ladder Macromolecular Systems. J. Am. Chem. Soc. 2005, 127 (25), 9105–9116. https://doi.org/10.1021/ja050184n.
- (17) Picini, F.; Schneider, S.; Gavat, O.; Vargas Jentzsch, A.; Tan, J.; Maaloum, M.; Strub, J.-M.; Tokunaga, S.; Lehn, J.-M.; Moulin, E.; Giuseppone, N. Supramolecular Polymerization of Triarylamine-Based Macrocycles into Electroactive Nanotubes. *J. Am. Chem. Soc.* 2021, 143 (17), 6498–6504. https://doi.org/10.1021/jacs.1c00623.
- (18) Ito, A. Macrocyclic Oligoarylamines as Hole- and Spin-Containing Scaffolds for Molecule-Based Electronics. *J. Mater. Chem. C* **2016**, *4* (21), 4614–4625. https://doi.org/10.1039/C6TC00973E.
- (19) Sakamaki, D.; Ito, A.; Tsutsui, Y.; Seki, S. Tetraaza[1 4]- and Octaaza[1 8]Paracyclophane: Synthesis and Characterization of Their Neutral and Cationic States. *J. Org. Chem.* **2017**, *82* (24), 13348–13358. https://doi.org/10.1021/acs.joc.7b02437.
- (20) Vale, M.; Pink, M.; Rajca, S.; Rajca, A. Synthesis, Structure, and Conformation of Aza[1 n]Metacyclophanes. J. Org. Chem. 2008, 73 (1), 27–35. https://doi.org/10.1021/jo702151n.
- (21) Ide, T.; Takeuchi, D.; Osakada, K.; Sato, T.; Higuchi, M. Aromatic Macrocycle Containing Amine and Imine Groups: Intramolecular Charge-Transfer and Multiple Redox Behavior. J. Org. Chem. 2011, 76 (22), 9504–9506. https://doi.org/10.1021/jo201650t.
- (22) Yang, T.-F.; Chiu, K. Y.; Cheng, H.-C.; Lee, Y. W.; Kuo, M. Y.; Su, Y. O. Studies on the Structure of N -Phenyl-Substituted Hexaaza[1 6] Paracyclophane: Synthesis, Electrochemical Properties, And Theoretical Calculation. J. Org. Chem. 2012, 77 (19), 8627–8633. https://doi.org/10.1021/jo301436g.
- (23) Kumar, P.; Yi, Z.; Zhang, S.; Sekar, A.; Soavi, F.; Cicoira, F. Effect of Channel Thickness, Electrolyte Ions, and Dissolved Oxygen on the Performance of Organic Electrochemical Transistors. *Appl. Phys. Lett.* 2015, 107 (5), 053303. https://doi.org/10.1063/1.4927595.
- (24) Mei, B.-A.; Munteshari, O.; Lau, J.; Dunn, B.; Pilon, L. Physical Interpretations of Nyquist Plots for EDLC Electrodes and Devices. J. Phys. Chem. C 2018, 122 (1), 194–206. https://doi.org/10.1021/acs.jpcc.7b10582.
- (25) Pickup, P. G. Alternating Current Impedance Study of a Polypyrrole-Based Anion-Exchange Polymer. *Faraday Trans.* **1990**, *86* (21), 3631. https://doi.org/10.1039/ft9908603631.
- (26) McDonald, M. B.; Hammond, P. T. Efficient Transport Networks in a Dual Electron/Lithium-Conducting Polymeric Composite for Electrochemical Applications. ACS Appl. Mater. Interfaces 2018, 10 (18), 15681–15690. https://doi.org/10.1021/acsami.8b01519.
- (27) Zayat, B.; Das, P.; Thompson, B. C.; Narayan, S. R. In Situ Measurement of Ionic and Electronic Conductivities of Conductive Polymers as a Function of Electrochemical Doping in Battery Electrolytes. J. Phys. Chem. C 2021, 125 (14), 7533-7541. https://doi.org/10.1021/acs.jpcc.0c08934.
- (28) Gul, S.; Shah, A.-H. A.; Bilal, S. Synthesis and Characterization of Processable Polyaniline Salts. J. Phys.: Conf. Ser. 2013, 439, 012002. https://doi.org/10.1088/1742-6596/439/1/012002.
- (29) Huang, W. S.; MacDiarmid, A. G. Optical Properties of Polyaniline. *Polymer* 1993, 34 (9), 1833–1845. https://doi.org/10.1016/0032-3861(93)90424-9.
- (30) Stejskal, J.; Kratochvíl, P.; Radhakrishnan, N. Polyaniline Dispersions 2. UV—Vis Absorption Spectra. Synthetic Met-

- als 1993, 61 (3), 225-231. https://doi.org/10.1016/0379-
- 6779(93)91266-5.
 (31) Stoll, S.; Schweiger, A. EasySpin, a Comprehensive Software Package for Spectral Simulation and Analysis in EPR. *Journal of Magnetic Resonance* **2006**, *178* (1), 42–55. https://doi.org/10.1016/j.jmr.2005.08.013.

TOC Artwork

